Band gap temperature-dependence and exciton-like state in copper antimony sulphide, CuSbS$_2$

Max Birkett, Christopher N. Savory, Mohana K. Rajpalke, Wojciech M. Linhart [iD], Thomas J. Whittles, James T. Gibbon [iD], Adam W. Welch, Ivona Z. Mitrovic, Andriy Zakutayev [iD], David O. Scanlon [iD], and Tim D. Veal [iD]

COLLECTIONS

Paper published as part of the special topic on Earth Abundant Materials in Solar Cells

View Online   Export Citation   CrossMark

ARTICLES YOU MAY BE INTERESTED IN

Research Update: Emerging chalcostibite absorbers for thin-film solar cells
APL Materials **6**, 084501 (2018); https://doi.org/10.1063/1.5027862

Band gap temperature-dependence of close-space sublimation grown Sb$_2$Se$_3$ by photo-reflectance
APL Materials **6**, 084901 (2018); https://doi.org/10.1063/1.5027157

Research Update: Bismuth-based perovskite-inspired photovoltaic materials
APL Materials **6**, 084502 (2018); https://doi.org/10.1063/1.5029484

Band gap temperature-dependence and exciton-like state in copper antimony sulphide, CuSbS₂

Max Birkett,[1,a] Christopher N. Savory,[2,3] Mohana K. Rajpalke,[4]
Wojciech M. Linhart,[5] Thomas J. Whittles,[1] James T. Gibbon,[1]
Adam W. Welch,[6] Ivona Z. Mitrovic,[7] Andriy Zakutayev,[6]
David O. Scanlon,[2,3,8] and Tim D. Veal[1,a]

[1]*Stephenson Institute for Renewable Energy, Department of Physics, Liverpool L69 7ZF, United Kingdom*
[2]*Department of Chemistry, University College London, Christopher Ingold Building, London WC1H 0AJ, United Kingdom*
[3]*Thomas Young Centre, University College London, Gower Street, London WC1E 6BT, United Kingdom*
[4]*Department of Electronic Systems, Norwegian University of Science and Technology, NO-7491 Trondheim, Norway*
[5]*Institute of Experimental Physics, Wroclaw University of Technology, 50-370 Wroclaw, Poland*
[6]*National Renewable Energy Laboratory, Material Science Center, Denver West Parkway, Golden, Colorado 80401, USA*
[7]*Department of Electrical Engineering and Electronics, University of Liverpool, Brownlow Hill, Liverpool L69 3GJ, United Kingdom*
[8]*Diamond Light Source Ltd., Diamond House, Harwell Science and Innovation Campus, Didcot OX11 0DE, United Kingdom*

The temperature-dependence of the band gap of the proposed photovoltaic absorber copper antimony sulphide (CuSbS₂) has been studied by Fourier-transform infrared spectroscopy. The direct gap rises from 1.608 to 1.694 eV between 300 and 4.2 K. Below 200 K an exciton-like feature develops above the absorption edge at 1.82 eV. First-principles calculations evaluate band structure, band symmetries, and dipole selection rules, suggesting distinctly enhanced absorption for certain excitonic optical transitions. Striking consistency is seen between predicted dielectric and absorption spectra and those determined by ellipsometry, which reveal rapidly strengthening absorption passing 10^5 cm^{-1} at 2.2 eV. These results suggest beneficial photovoltaic performance due to strong optical absorption arising from unusually strong electron–hole interactions in polycrystalline CuSbS₂ material. © *2018 Author(s).*
All article content, except where otherwise noted, is licensed under a Creative Commons Attribution (CC BY) license (http://creativecommons.org/licenses/by/4.0/) https://doi.org/10.1063/1.5030207

In recent years, the leading technologies for thin-film photovoltaics (TFPV) have achieved performance parity with polycrystalline silicon, with both types reaching 21% cell efficiencies.[1] The careful selection of excellent optical absorbers, some 100× stronger than silicon,[2] combined with deposition processes matured in the display-industry, gives thin-film modules various cost benefits over crystalline silicon and three times better energy payback times.[4]

Yet the leading technologies for thin-film photovoltaics, cadmium telluride (CdTe) and copper indium gallium diselenide, Cu(In, Ga)Se₂ (or CIGS), each have commercial limitations which complicate increasing total installed capacity beyond 100 GWp, just a fraction[2] of the multi-terawatt PV market envisaged by 2050. Tellurium, gallium, and indium are relatively expensive,[4] indium and tellurium (particularly) are scarce with limited geographical availability,[5] and concerns remain over cadmium toxicity.[6–9] All this drives research into earth-abundant and non-toxic absorber materials

---

[a]Authors to whom correspondence should be addressed: max.birkett@gmail.com and T.Veal@liverpool.ac.uk

with desirable properties for thin-film PV: strong optical absorption with an optimal band gap, limited non-radiative recombination, and favorable carrier dynamics.[10,11]

Rather than seeking entirely new systems, one approach is to adapt presently successful systems (such as CIGS) by replacing problem elements.[2] In particular, the layered ternary transition-metal dichalcogenides (TMDCs) have received attention[12] both due to chemical similarities to CIGS and for other benefits, such as strong absorption (somewhat better than CIGS)[10,13] and attractive costs.[14,15] The low-cost, earth-abundant, and non-toxic semiconductor copper antimony disulphide ($CuSbS_2$ or chalcostibite) has a reported near-optimal 1.5 eV direct band gap and strong optical absorption rising from 10^4 to 10^5 cm^{-1} between 1.6 and 1.8 eV.[6,16,17] The crystal comprises alternating layers of Cu- and Sb-sheets normal to the *c*-axis.[18] Natively *p*-type, due to shallow acceptor-like V_{Cu} and V_S vacancies and anti-site Cu_{Sb} defects,[17,19] carrier concentration is tunable from 10^{16} to 10^{18} cm^{-3} through growth parameters.[6] Fortunately, these defect states are occupied at 300 K, blocking recombination via these centers and (as the indirect transition is near Γ) permitting conduction-band minimum to valence-band maximum radiative-recombination: rather unusual in indirect semiconductors as non-radiative recombination usually dominates.[19] Despite favorable properties, $CuSbS_2$ cells have so far shown unimpressive record efficiencies (3.2%);[20] however, the ubiquitous $CdS/CuSbS_2/Mo$ architecture (inherited from CIGS) is now thought to introduce significant detrimental band offsets with CdS and Mo;[21,22] thus, superior performance is expected with alternative window layers and back contacts (perhaps also conveniently disposing of Cd-toxicity concerns).

$CuSbS_2$ has a stable orthorhombic phase (space group *Pnma*) below 550 °C with good thermal, environmental, and electrical stability.[16,17,23,24] Synthesis of phase-pure $CuSbS_2$ is complicated by the many phases of the Cu–Sb–S system.[9,24] Four ternary phases can be observed in thermal equilibrium: $CuSbS_2$ (chalcostibite), $Cu_{12}Sb_4S_{13}$ (tetrahedrite), Cu_3SbS_3 (skinnerite), and Cu_3SbS_4 (famatinite). Other phases observed during growth include[6] Sb_2S_3 (stibnite), $Cu_{1.8}S$ (digenite), Cu_2S, and CuS. Recently, a growth window (the *self-regulated* regime) favoring synthesis of stoichiometric and phase-pure $CuSbS_2$ material has been found.[6,25] The window is bounded by an Sb_2S_3 secondary phase at low temperature (which sublimes away above ~350 °C) and by the upper limit for stoichiometric growth at 400 °C (where $CuSbS_2$ decomposes into $Cu_{12}Sb_4S_{13}$). Prior synthesis methods fall into two categories. In the first class, $CuSbS_2$ is formed directly and material quality may be further refined by subsequent annealing. Examples include spray pyrolysis,[26] thermal evaporation,[14] chemical bath deposition,[16,17] magnetron co-sputtering,[6] and solvothermal synthesis.[27] In the second class, layers of Cu and Sb compounds are deposited and then transformed into homogeneous $CuSbS_2$ material in a secondary sulphurisation process. Methods include the chemical bath deposition (CBD) of CuS/Sb_2S_3 layers,[28] the combined CBD and thermal evaporation of Cu/Sb_2S_3 layers,[15] and the thermal evaporation or DC sputtering of a Cu/Sb stack.[9,29]

After confirming the phase-purity of the polycrystalline, radio-frequency (RF) magnetron co-sputter-grown $CuSbS_2$ films, this work reports the temperature-dependence of the direct band gap between 4.2 and 300 K by Fourier-transform infrared spectroscopy (FTIR) and investigates a low-temperature exciton-like absorption feature. Refractive index and absorption spectra are determined by spectroscopic ellipsometry. Density functional theory (DFT) band structures and dipole selection rules are calculated to provide tools which help to explain the exciton-like absorption feature.

Polycrystalline *p*-type $CuSbS_2$ films ($p \sim 10^{16}$–10^{17} cm^{-3}) were deposited on glass substrates (Corning Eagle XG, an alkaline earth boro-aluminosilicate glass)[30] by radio-frequency (RF) magnetron co-sputtering of Cu_2S and Sb_2S_3 targets in a 3 mTorr Ar atmosphere. Deposition occurred within the *self-regulated* regime growth window, as discussed above and in detail elsewhere.[6,25]

The $CuSbS_2$ *Pnma* phase was confirmed using a Panalytical X'pert Pro x-ray diffractometer (XRD) with an unmonochromated 40 kV copper anode and point detector, using a θ:2θ scan between 10° and 55° 2θ at 300 K and 0.15° min^{-1}. Scanning electron microscopy (SEM) at 10 keV with a JEOL JSM 7001F showed films with uniform coverage and a non-specific granular morphology (see supplementary material Fig. 1). Cross-sectional SEM showed an average 570 nm film thickness. Energy dispersive spectrometry (EDS) using an Oxford Instruments INCA x-act silicon drift detector showed prominent Cu, Sb, and S lines with no contaminants. Infrared transmission and specular reflection spectra were acquired at 11° angle of incidence for 17 temperatures between 4.2 and 300 K and photon energies of 0.3–2.4 eV using a Bruker Vertex 70v Fourier-transform infrared

(FTIR) spectrometer with a combined reflection-transmission accessory and an Oxford Instruments CFV2 continuous-flow helium cryostat. The dielectric function was also evaluated from 0.7 to 5.1 eV at 300 K with a Woollam M-2000-UI (rotating compensator) spectroscopic ellipsometer at incident angles of 65°, 70°, and 75°. A film-substrate B-spline dielectric model comprising surface roughness was fitted to the reflection, transmission, and depolarization data in *CompleteEASE* v5.08.[31]

Density functional theory (DFT) calculations were performed in the VASP code[32–35] with the screened HSE06 hybrid density functional,[36–38] and scalar relativistic pseudopotentials. Core and valence electron interactions were described by projector augmented waves (PAWs).[39,40] Calculations used a plane-wave cutoff energy of 350 eV (increased by 30% on optimization to account for Pulay stresses), a Γ-centered $4 \times 7 \times 2$ mesh ($8 \times 14 \times 4$ for optical properties), and a geometry convergence criterion of 0.01 eV Å^{-1}. Evaluation of the high-frequency dielectric function used the method of Gajdoš *et al.*[41] Eigenfunctions for symmetry analysis were expanded in a plane-wave basis (952 eV cut-off energy) in the ABINIT code,[42,43] with the PBE96 generalized gradient approximation[44] (GGA) and Troullier–Martins pseudopotentials.[45] Studies selected a $8 \times 13 \times 4$ mesh with 56 k-points in the irreducible Brillouin zone, achieving total energy convergence to better than 0.01%.

As the $CuSbS_2$ optical properties may be crystallinity- and orientation-dependent, XRD was performed to confirm the *Pnma* phase and to assess any texture or impurity phases. Supplementary material Fig. 2 shows Rietveld refinement[46] of the $CuSbS_2$ *Pnma* structure (via *FullProf* v5.70),[47] giving lattice parameters $a = 6.0210(23)$ Å, $b = 3.793(4)$ Å, and $c = 14.496(6)$ Å, broadly consistent with prior studies.[27,48–50] This work also indicated that the film is essentially phase pure (discussed further in supplementary material Sec. II). Some excess residuals indicated preferential orientation, best-fit with a (200)-texture with intensities modeled as $\exp\left(-G\alpha_{hkl}^2\right)$, where $G = 0.55(8)$ and α_{hkl} is the acute angle between the (hkl) and (200) plane normals.

The ellipsometric refractive index and absorption spectra are shown in Fig. 1(a) and the FTIR reflectivity $R_t(\hbar\omega)$ and transmissivity $T_t(\hbar\omega)$ spectra are shown in supplementary material Fig. 3. The transmission spectra show an absorption edge near 1.6 eV with a strong temperature-dependence. Below 1.6 eV, the reflectivity spectra show oscillations from coherent internal reflections not seen in the transmissivity, either as coherence is destroyed by thickness variations in the borosilicate substrate or due to sub-gap extinction in the film (at least three optical path lengths are required to observe oscillations in the transmissivity). The reflectivity and transmissivity spectra are reduced to absorption spectra $\alpha(\hbar\omega)$ using equations describing the reflection and transmission of light directed at normal incidence at a single incoherent optical layer of thickness d with parallel faces

$$R_t = R\left[1 + \frac{(1-R)^2 \exp(-2\alpha d)}{1 - R^2 \exp(-2\alpha d)}\right] \quad \text{and} \quad T_t = \frac{(1-R)^2 \exp(-\alpha d)}{1 - R^2 \exp(-2\alpha d)}, \quad (1)$$

where $R(\hbar\omega)$ is the (unmeasured) intrinsic reflectivity at a semi-infinite boundary between the vacuum and the $CuSbS_2$ film (by contrast, the total reflectivity R_t includes the contributions from internal reflections at each face). The intrinsic reflectivity R must be determined before proceeding: this procedure has been discussed in detail previously.[51] This fitting used the sample thickness of 570 nm, as indicated from SEM and ellipsometry. Figure 1(b) shows the resulting absorption spectra.[52] The absorption edge increases relatively steeply (as desired for photovoltaic absorbers) and redshifts with increasing temperature. An interesting temperature-dependent absorption feature is present in Fig. 1(b) at 1.82 eV and is discussed shortly. While the FTIR and SE absorption coefficients agree above the onset (9×10^4 cm^{-1} at 2 eV), subgap reflections in the FTIR spectra lead to differences ($\alpha_{FTIR} \sim 10^4$ cm^{-1} or $\alpha_{SE} = 4 \times 10^4$ cm^{-1}) below the onset.

First-principles band structure calculations suggest that while the fundamental absorption in $CuSbS_2$ is indirect, a direct onset (associated with an M_0 critical point) exists to only 50 meV higher energy. Given that the absorption strength at indirect onsets is typically orders of magnitude weaker than that for direct transitions, the absorptions edges of Fig. 1(b) are fitted with functions describing absorption due to a direct transition with an Urbach tail at an M_0 critical point,

$$\alpha_d = \frac{A}{\hbar\omega}\sqrt{R\left(\hbar\omega - E_g^d\right)} \quad \text{and} \quad \alpha_U(\hbar\omega) = B\exp\left(\gamma\left\{\hbar\omega - E_g^d - E_U\right\}\right), \quad (2)$$
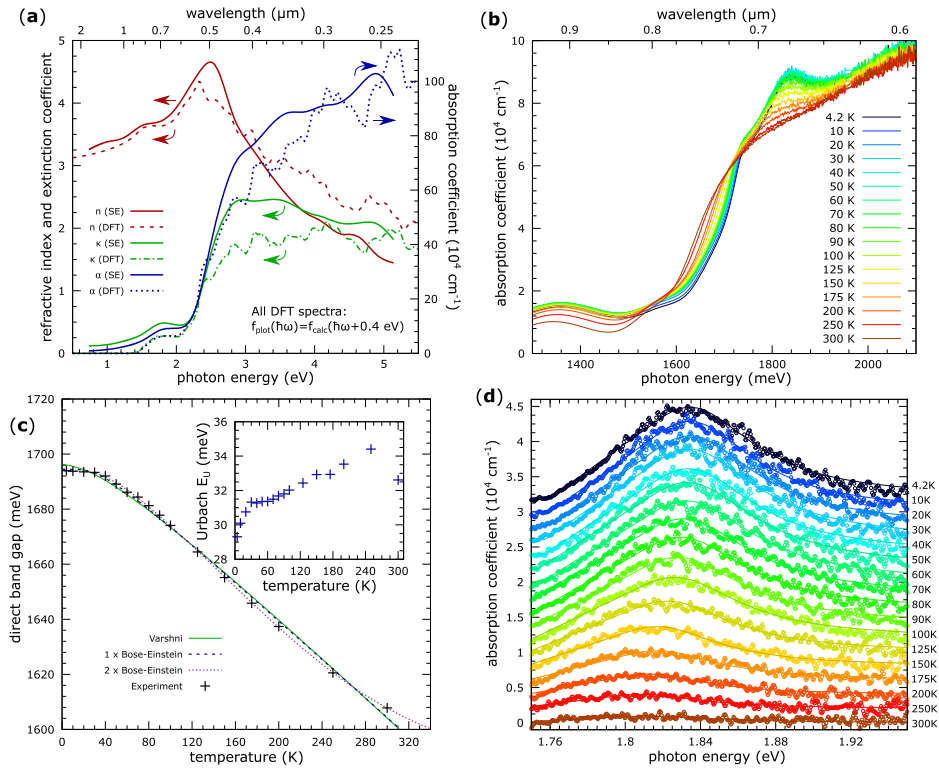
FIG. 1. (a) Complex refractive index ($\tilde{n} = n + i\kappa$) and absorption spectra via DFT (HSE06) and ellipsometry at 300 K. Plotted DFT spectra are down-shifted by 0.4 eV (likely due to electron–hole interactions, see the text) revealing a good match with the experimental spectra. (b) FTIR absorption spectra; between 4.2 and 300 K, the absorption edge redshifts by some 50 meV. An interesting feature develops at low temperatures near 1.83 eV. (c) Temperature-dependence of the optical gap, fitted with the Varshni relation, and one and two Bose–Einstein oscillators. The inset shows an Urbach tail which grows with temperature. (d) The temperature-dependent feature after removal of the absorption onset (traces displaced vertical for clarity). The line position and intensity each increase with decreasing temperature; no feature is seen at 300 K. Note the asymmetric line shape which comprises a Lorentzian high-energy edge (and peak) with a linear low-energy edge.

where E_g^d is the direct band gap, A and E_U are material-dependent parameters, B and γ are functions only of these parameters as discussed in Ref. 51, and $R(\cdot)$ denotes the ramp function: $R(x) = x$ for $x > 0$, else $R(x) = 0$. The absorption associated with a direct onset is then $\alpha_U(\hbar\omega)$ for $\hbar\omega \leq \left(E_g^d + E_U\right)$ and $\alpha_d(\hbar\omega)$ otherwise. Figure 1(c) shows the results of fitting (2) to the experimental absorption edges: the direct gap rises from 1.608 to 1.694 eV between 300 and 4.2 K, while the Urbach parameter E_U rises from 29.3 to 32.6 meV (an average absorption baseline was evaluated between 1.13 and 1.46 eV for each spectrum, while the direct gap and Urbach energy E_U were constrained to lie, respectively, between 1.5 and 2.0 eV and below 0.1 eV).

The band gap temperature-dependence $E_g(T)$ of Fig. 1(c) is fitted with the Varshni relation as[53]

$$E_g^{\text{Varshni}} = E_0 - \frac{\alpha T^2}{T + \beta} \quad (3)$$

and with models comprising one and two Bose-Einstein oscillators as[54–56]

$$E_g^{BE} = B + \sum_i \alpha_i \left[1 + \frac{2}{\exp\left(\frac{E_i}{k_B T}\right) - 1} \right]. \quad (4)$$

The results of the least-squares fits are shown as the solid and broken lines in Fig. 1(c). The Varshni fit suggests respective E_0, α, and β parameters of 1.70 eV, 0.37 meV K^{-1}, and 63.2 K, while the single Bose–Einstein oscillator fit finds a zero Kelvin gap of 1.71 eV with reasonable respective average phonon and electron–phonon interaction energies (E_i and α_i) of 8.4 and −17.3 meV.
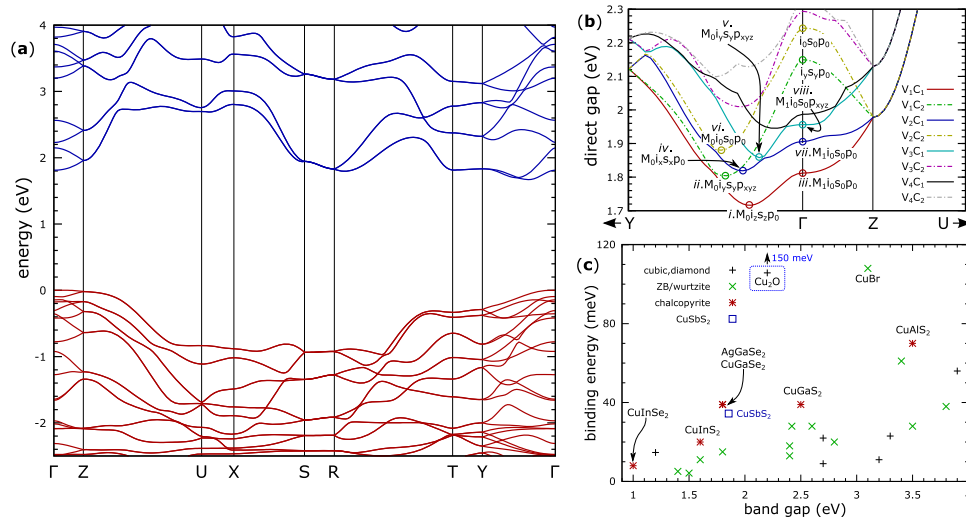
FIG. 2. (a) HSE06 band structure. (b) Lowest critical points in the HSE06 band structure annotated with selection rules for optical transitions (between GGA wavefunctions); the topmost valence bands (V_1 descending through V_4) are subtracted from the lowest conduction bands (C_1 increasing through C_4) giving the direct gaps near Γ. The lowest critical points (M_0 and M_1 Van Hove singularities) and dipole selection rules are given: i, s, and p, respectively, denote interband and excitonic s- and p-transitions, while the subscripts denote the required light-polarization direction. (c) Exciton binding energies versus band gap: a 3D Wannier–Mott exciton with 34 meV binding energy (1.85 eV gap) is hypothesized at the M_0 critical point (ii) in $CuSbS_2$ and is reasonably consistent with the trend found in chalcopyrite systems.

The double Bose–Einstein oscillator fit, which caters for the different energy scales expected for acoustic and optical phonons, suggests a base parameter B of 1.15 eV and respective average phonon and interaction energies $\{E_i, \alpha_i\}$ of $\{11.3, -26.80\}$ and $\{117.9, 567.35\}$ meV.

A temperature-dependent feature is evident at 1.82 eV just above the fundamental absorption edges of Fig. 1(b). With decreasing temperature, the feature narrows, increases in prominence, and shifts to higher photon energies, becoming particularly obvious below 150 K. Below 200 K, a definite shoulder separates the feature from the absorption edge, suggesting a transition between states separated by more than the fundamental band gap. At 4.2 K, where Fig. 1(c) shows a 1.694 eV direct gap, the feature has shifted to 1.83 eV. The feature is seen in Fig. 1(d) after removal of the fundamental absorption using the shoulder and above-feature absorption magnitudes (discussed in supplementary material Sec. IV). An asymmetric line shape emerges: the low-energy edge is near-linear, while the high-energy edge is approximately Lorentzian. Asymmetric Lorentzian or Gaussian line shapes are typically seen in the discrete line spectra of excitons.[57,58] To fit the temperature evolution, a quasi-Lorentzian was constructed with a Lorentzian line shape $L(x; x_0, \Gamma)$ (centered at x_0, width Γ) above $x_0 - \Lambda$, with the parameter Λ controlling a smooth and continuous transition from Lorentzian form to a linear edge (see supplementary material Sec. V). The solid lines in Fig. 1(d) denote the line fits, while the temperature-dependence of the line-position is seen more clearly in supplementary material Fig. 4.

As the temperature evolution seen in Fig. 1(d) and supplementary material Fig. 4 is highly typical of band structure temperature dependence from thermal expansion and electron–phonon interactions, the solid lines in supplementary material Fig. 4 denote fits with the Varshni relation (3), giving $\{E_0, \alpha, \beta\}$ of 1.8349(4) eV, 0.18(3) meV K^{-1} and 120(50) K, and with a single Bose–Einstein oscillator (4), giving parameters $\{B, E_{\text{ph}}, \alpha_{\text{ep}}\}$ of 1.8406(16) eV, 7.6 ± 2.2 meV and $-12(4)$ meV. Of these, the Bose–Einstein oscillator best describes the data with a sensible averaged phonon energy E_{ph}; indeed, the fitted averaged phonon and electron–phonon energies are consistent with those determined for the double Bose–Einstein oscillator (assuming a 10% uncertainty for the latter).

Figure 2(a) and supplementary material Fig. 5, respectively, show the HSE06 and GGA band structures, revealing highly similar dispersion. The fundamental HSE06 band gap is indirect at 1.67 eV, yet a 1.72 eV direct gap at reciprocal space point $(0, 0.156, 0)$ (along Γ-Y) is consistent with

the 1.70 eV Varshni 0 K gap; the direct gap at Γ is somewhat higher at 1.81 eV. Band edge effective masses $\{m_h^{\Gamma \to Y}, m_h^{\Gamma \to Z}, m_e^{Y-\Gamma}\}$ of $\{2.5, 9.4, 0.6\}$ are found. The HSE06 direct gap is more clearly seen in Fig. 2(b), in which the topmost HSE06 valence bands are subtracted from the lowest conduction bands to show the nature of relevant M_0 and M_1 critical points, annotated with GGA-calculated selection rules for dipole interband and excitonic transitions. With spin-orbit coupling, the band gap reduces by just 30 meV, yet the dispersion is essentially unchanged (see supplementary material Fig. 6). While (Cu-*d*, S-*p*) and (Sb-*p*, S-*p*) states dominate the valence and conduction bands,[22] the usual spin-orbit splitting atomic number z^4 dependence (derived from neutral atomic wavefunctions) is perhaps weakened for cationic Sb compounds: similarly negligible splittings are found in the binary Sb chalcogenides[59] and chalcohalides.[60] Band symmetries are determined from their characters χ computed from the inner product $\langle \psi_{n\mathbf{k}}|\{R, \tau\}\psi_{n\mathbf{k}}\rangle = \chi$, where a *Pnma* space group operation $\{R, \tau\}$ acts on the relevant normalized real-space GGA wavefunctions $\psi_{n\mathbf{k}}(\mathbf{r})$ (see supplementary material Sec. VI). Using the Kohn–Sham wavefunctions and eigenvalues in this manner is somewhat without rigorous justification, particularly for excited states; however, such symmetry arguments are often made to assess potential PV absorbers.[10,11] Figure 1(a) shows that the HSE06 dielectric spectra match the ellipsometric spectra after a 0.4 eV redshift; such shifts are associated with the omission of electron–hole interactions, which generally redistribute higher-energy transitions to lower energies,[51,61–63] giving redshifts ranging from 0.5 eV in InN to ~2 eV in ionic materials or those with weak dielectric screening.[61,64] Associating the fundamental interband absorption with the lowest dipole-allowed M_0 critical point (i) in Fig. 2(b), the feature in Fig. 1(d) might then arise from atypical interband absorption, optically active impurity or defect states, or excitonic resonances. While similar absorption maxima are seen at non-excitonic interband transitions at M_1 critical points,[65] several of which are labeled in Fig. 2(b), vanishing reduced masses at room temperature (giving zero joint density of states) are necessary to suppress the feature as in Fig. 1(d). As impurity, defect, and excitonic states share many characteristics, and given the line shape, temperature-dependence, dielectric spectral downshift, and numerous critical points labeled in Fig. 2(b), the hypothesis emerges that the feature may be an exciton associated with an M_0 or M_1 critical point at $(E_g + 0.1 \text{ eV})$ between Γ and Y.

M_0 transitions i, ii, iv, and v in Fig. 2(b) allow *s*-states for only one polarization direction, leading to one-third intensity in polycrystalline material; transitions ii and v at E_g + 90 and 140 meV *also* allow *p*-states for all polarizations and may be inseparable in Fig. 1(d). A binding energy R_x of 34 meV is found for a Wannier–Mott exciton associated with (ii) (see supplementary material Sec. VIII) with $n = 1$, a dielectric constant $\epsilon_r(1.82 \text{ eV}) = 13.7$ from Fig. 1(a), and a fitted HSE06 reduced mass of $\mu = 0.47\, m_e$. This gives a 1.5 nm exciton Bohr radius, which averages over 47 unit cells, supporting the Wannier–Mott treatment. Saddle-point or hyperbolic excitons at M_1 critical points also show enhanced absorption: controversial due to their metastability but feasible under large negative reduced masses,[66,67] such 2D excitons have $n = 0$ lines eight times stronger than those in the 3D exciton.[65] A 2D exciton with allowed *p*-like states for all polarizations and 85 meV binding energy is found for the viii transition (with $n = 0$) with the largest M_1 reduced mass ($\mu_z = 1.6$). Thus, enhanced absorption features may result from specific excitons in polycrystalline CuSbS$_2$.

Typical band gap temperature-evolution and Varshni parameters are seen, when compared to respective mean (and standard deviation) α and β values of 0.6(5) meV K^{-1} and 400(500) K for fits to 37 common semiconductors.[53,68] Consistent respective Varshni and HSE06 direct gaps of 1.70 eV and 1.72 eV are found at 0 K. Material quality and experimental issues lead to some variability in reported CuSbS$_2$ band gaps: annealing often improves crystallinity (clearly seen in temperature-dependent photoluminescence defect studies)[19] leading to band gap changes, while reliable band gap determination depends particularly on careful handling of Urbach tails (e.g., see Ref. 69). Accurate band gaps are crucial for assessing band-alignment and solar cell optimization; recent reports seem to be converging on a 1.6 eV direct gap at 300 K.[70–72]

The layered 2D nature of TMDCs leads to significantly enhanced electron–hole interactions and prominent excitonic optical features, often revealed in monolayer studies due to spatial confinement and reduced screening effects.[73,74] Excitonic features also dominate absorption spectra in other layered systems, such as few-layer black phosphorus.[75] Claims of excitons in CuSbS$_2$ are perhaps unsurprising given the rich display of exciton phenomena in the (tetragonal) Cu-III-VI$_2$

chalcopyrites,[76] see Fig. 2(c) which also suggests a reasonable $CuSbS_2$ exciton position. The highest temperature at which the feature shows significant absorption is 200 K, the average thermal energy $\frac{3}{2}k_BT$ here being 26 meV, 76% of the 34 meV exciton binding energy; however, exciton visibility is mainly determined by interactions with the optical phonon population,[77] described by Bose–Einstein statistics. With an 11 meV phonon energy (fitted on p. 4), the phonon occupation number exceeds unity before 200 K, which qualitatively supports the absence of exciton features beyond this temperature. The significance of selection rules for dipole transitions in orthorhombic crystals is demonstrated by $AgInS_2$ (space group $Pna2_1$) where transitions to the Γ_1 conduction band are allowed only from Γ_4 and Γ_1 valence bands (respectively, for z- and y-polarized light), while transitions to exciton s-states are allowed from Γ_1, Γ_2 and Γ_4 valence bands with z-polarized light only.[78,79] Above absorption edge excitons are not uncommon,[80] particularly when associated with transitions from split-off valence bands, e.g., absorption spectra of the layered compound InSe show excitons linked to the 1.35 eV band gap and also at 2.6 and 2.9 eV (lines E1′ and E1) due to split-off valence bands.[81] Above gap excitons are also seen in other TMDCs:[82] absorption spectra of $2H\text{-}MoS_2$ show two 2D exciton lines (A and B) occurring below and above the band gap and again associated with a 0.2 eV spin-orbit split valence band.[83] Because optical transitions conserve the spin of the excited carrier and the spatial parts of the wavefunctions may possess different symmetries, the exciton selection rules involving spin-orbit split bands may be more restrictive.[84]

Photovoltaic devices should benefit if polycrystalline $CuSbS_2$ has strong excitonic effects: as the electron–hole interaction significantly enhances absorption strength even when no discrete exciton lines are seen, i.e., at room temperature.[65] While the interaction has detrimental charge separation effects in systems with strongly bound (Frenkel) excitons,[85] an electron, hole, and exciton plasma model developed in supplementary material Sec. X finds a negligible fraction of bound excitons in $CuSbS_2$ at 300 K, supporting the absence of discrete exciton features in the 300 K absorption spectrum of Fig. 1(b). As the electron–hole interaction is neglected in nearly all first-principles calculations, this perhaps cautions against relying on first-principles methods in isolation. Because orthorhombic crystals have biaxial optical behavior, i.e., optical properties which differ in all three spatial directions,[86] further optical investigations with oriented single crystals and light polarized parallel and perpendicular to the crystal axes would be of great interest. Such work may stimulate optimization of crystallite orientation to maximize optical absorption. The critical points of Fig. 2(b) suggest four different interband transitions within 200 meV which may be discriminated as a function of light polarization, and the excitonic feature at 1.82 eV should be easier to resolve under such experimental conditions. The feature has a good line shape at 80 K and so should be conveniently accessible at liquid nitrogen temperature.

In conclusion, the direct gap of phase-pure, polycrystalline RF magnetron co-sputter-grown $CuSbS_2$ is found to rise from 1.608 to 1.694 eV between 300 and 4.2 K by FTIR spectroscopy. The 1.70 eV Varshni gap at 0 K supports the 1.72 eV direct gap found in first-principles HSE06 calculations. A potential excitonic feature is seen at 1.82 eV below 200 K; selection rule evaluation suggests that this may result from distinctly enhanced absorption for certain exciton transitions.

See supplementary material for further details on film morphology, phase analysis, FTIR reflection and transmission spectra, fitting of the exciton-like feature, GGA and HSE06 band structures (with spin-orbit coupling) and band symmetries, irreducible representations, and selection rules for interband and excitonic transitions. Additionally, a free-electron, free-hole, and bound-exciton model is developed to estimate the exciton number fraction at thermodynamic equilibrium and resultant consequences for photovoltaic carrier-separation.

[1] M. A. Green, K. Emery, Y. Hishikawa, W. Warta, and E. D. Dunlop, Prog. Photovoltaics: Res. Appl. **23**, 1 (2015).

[2] D. W. Lane, K. J. Hutchings, R. McCracken, and I. Forbes, in *Materials Challenges: Inorganic Photovoltaic Solar Energy*, 1st ed. (Royal Society of Chemistry, 2015), Chap. 6, pp. 160–208.

[3] B. Mattson, "7 reasons thin film is alive and set to win in solar," https://www.renewableenergyworld.com/articles/2014/07/7-reasons-thin-film-is-alive-and-set-to-win-in-solar.htm (2014).

[4] U. S. Geological Survey, *Mineral Commodity Summaries 2016* (U.S. Geological Survey, 2016), ISBN: 9781411340114.

[5] USGS estimated global Si, Ga, In and Te production in 2015 was as follows: 8100000, 600, 755 and 120 t.[4]

[6] A. W. Welch, P. P. Zawadzki, S. Lany, C. A. Wolden, and A. Zakutayev, Sol. Energy Mater. Sol. Cells **132**, 499 (2015).

[7] D. J. Temple, A. B. Kehoe, J. P. Allen, G. W. Watson, and D. O. Scanlon, J. Phys. Chem. C **116**, 7334 (2012).

[8] M. Kumar and C. Persson, J. Renewable Sustainable Energy **5**, 031616 (2013).

[9] E. Peccerillo, J. Major, L. Phillips, R. Treharne, T. J. Whittles, V. Dhanak, D. Halliday, and K. Durose, in *Photovoltaic Specialist Conference (PVSC)* (IEEE, 2014), p. 0266.

[10] L. Yu, R. S. Kokenyesi, D. A. Keszler, and A. Zunger, Adv. Energy Mater. **3**, 43 (2013).

[11] L. Yu and A. Zunger, Phys. Rev. Lett. **108**, 068701 (2012).

[12] A. M. Ganose, C. N. Savory, and D. O. Scanlon, Chem. Commun. **53**, 20 (2017).

[13] C. Tablero, J. Phys. Chem. C **119**, 8857 (2015).

[14] A. Rabhi, M. Kanzari, and B. Rezig, Thin Solid Films **517**, 2477 (2009).

[15] R. Ornelas-Acosta, S. Shaji, D. Avellaneda, G. Castillo, T. D. Roy, and B. Krishnan, Mater. Res. Bull. **61**, 215 (2015).

[16] S. M. Salem, M. B. S. Osman, A. M. Salem, G. B. Sakr, H. M. Hashem, and I. M. E. Radaf, J. Appl. Sci. Res. **9**(2), 1083 (2013).

[17] B. Yang, L. Wang, J. Han, Y. Zhou, H. Song, S. Chen, J. Zhong, L. Lv, D. Niu, and J. Tang, Chem. Mater. **26**, 3135 (2014).

[18] K. Ramasamy, H. Sims, W. H. Butler, and A. Gupta, J. Am. Chem. Soc. **136**, 1587 (2014).

[19] F. Willian de Souza Lucas, H. Peng, S. Johnston, P. C. Dippo, S. Lany, L. H. Mascaro, and A. Zakutayev, J. Mater. Chem. A **5**, 21986 (2017).

[20] S. Banu, S. J. Ahn, S. K. Ahn, K. Yoon, and A. Cho, Sol. Energy Mater. Sol. Cells **151**, 14 (2016).

[21] A. W. Welch, L. L. Baranowski, P. Zawadzki, C. DeHart, S. Johnston, S. Lany, C. A. Wolden, and A. Zakutayev, Prog. Photovoltaics: Res. Appl. **24**, 929 (2016).

[22] T. J. Whittles, T. D. Veal, C. N. Savory, A. W. Welch, F. W. de Souza Lucas, J. T. Gibbon, M. Birkett, R. J. Potter, D. O. Scanlon, A. Zakutayev, and V. R. Dhanak, ACS Appl. Mater. Interfaces **9**, 41916 (2017).

[23] M. Kumar and C. Persson, Energy Procedia **44**, 176 (2014).

[24] A. Sugaki, H. Shima, and A. Kitakaze, "Phase relations of the Cu_2S-Sb_2S_3 system," Tech Rep. Yamaguchi University **1**, 169 (1973).

[25] A. W. Welch, "CuSb(S, Se)$_2$ thin film heterojunction photovoltaic devices," Ph.D. thesis, Colorado School of Mines, USA, 2015.

[26] S. Manolache, A. Duta, L. Isac, M. Nanu, A. Goossens, and J. Schoonman, Thin Solid Films **515**, 5957 (2007).

[27] J. Zhou, G.-Q. Bian, Q.-Y. Zhu, Y. Zhang, C.-Y. Li, and J. Dai, J. Solid State Chem. **182**, 259 (2009).

[28] Y. Rodriguez-Lazcano, M. Nair, and P. Nair, J. Cryst. Growth **223**, 399 (2001).

[29] D. Colombara, "Investigation of chalcogenide absorber materials for photovoltaic applications," Ph.D. thesis, Department of Chemistry, University of Bath, 2012.

[30] Corning, Inc., "Corning Eagle XG product information sheet" (Corning Display Technologies, 2013), www.corning.com, url: http://bit.ly/292BUPK.

[31] J. A. Woollam Co., *Complete EASE Ellipsometry Software* (J. A. Woollam Co., Inc., 2014).

[32] G. Kresse and J. Furthmüller, Phys. Rev. B **54**, 11169 (1996).

[33] G. Kresse and J. Hafner, Phys. Rev. B **49**, 14251 (1994).

[34] G. Kresse and J. Hafner, Phys. Rev. B **47**, 558 (1993).

[35] G. Kresse and J. Furthmüller, Comput. Mater. Sci. **6**, 15 (1996).

[36] J. Heyd, G. E. Scuseria, and M. Ernzerhof, J. Chem. Phys. **118**, 8207 (2003).

[37] J. E. Peralta, J. Heyd, G. E. Scuseria, and R. L. Martin, Phys. Rev. B **74**, 073101 (2006).

[38] A. V. Krukau, O. A. Vydrov, A. F. Izmaylov, and G. E. Scuseria, J. Chem. Phys. **125**, 224106 (2006).

[39] P. E. Blöchl, Phys. Rev. B **50**, 17953 (1994).

[40] G. Kresse and D. Joubert, Phys. Rev. B **59**, 1758 (1999).

[41] M. Gajdoš, K. Hummer, G. Kresse, J. Furthmüller, and F. Bechstedt, Phys. Rev. B **73**, 045112 (2006).

[42] X. Gonze, B. Amadon, P.-M. Anglade, J.-M. Beuken, F. Bottin, P. Boulanger, F. Bruneval, D. Caliste, R. Caracas, M. Côté, T. Deutsch, L. Genovese, P. Ghosez, M. Giantomassi, S. Goedecker, D. R. Hamann, P. Hermet, F. Jollet, G. Jomard, S. Leroux, M. Mancini, S. Mazevet, M. J. T. Oliveira, G. Onida, Y. Pouillon, T. Rangel, G.-M. Rignanese, D. Sangalli, R. Shaltaf, M. Torrent, M. J. Verstraete, G. Zerah, and J. W. Zwanziger, Comput. Phys. Commun. **180**, 2582 (2009).

[43] M. Fuchs and M. Scheffler, Comput. Phys. Commun. **119**, 67 (1999).

[44] J. P. Perdew, K. Burke, and M. Ernzerhof, Phys. Rev. Lett. **77**, 3865 (1996).

[45] N. Troullier and J. L. Martins, Phys. Rev. B **43**, 1993 (1991).

[46] H. M. Rietveld, J. Appl. Crystallogr. **2**, 65 (1969).

[47] J. Rodríguez-Carvajal, Phys. B **192**, 55 (1993).

[48] W. Hofmann, Z. Kristallogr. **84**, 177 (1933).

[49] A. Kyono and M. Kimata, Am. Mineral. **90**, 162 (2005).

[50] M. F. Razmara, C. M. B. Henderson, R. A. D. Pattrick, A. M. T. Bell, and J. M. Charnock, Mineral. Mag. **61**, 79 (1997).

[51] M. Birkett, C. N. Savory, A. N. Fioretti, P. Thompson, C. A. Muryn, A. D. Weerakkody, I. Z. Mitrovic, S. Hall, R. Treharne, V. R. Dhanak, D. O. Scanlon, A. Zakutayev, and T. D. Veal, Phys. Rev. B **95**, 115201 (2017).

[52] The 4.2 and 300 K absorption edges (excluding the possible excitonic state) were published previously in Ref. 22.

[53] Y. P. Varshni, Physica **34**, 149 (1967).

[54] J. Bhosale, A. K. Ramdas, A. Burger, A. Muñoz, A. H. Romero, M. Cardona, R. Lauck, and R. K. Kremer, Phys. Rev. B **86**, 195208 (2012).

[55] C. Yu, Z. Chen, J. J. Wang, W. Pfenninger, N. Vockic, J. T. Kenney, and K. Shum, J. Appl. Phys. **110**, 063526 (2011).

[56] A. Göbel, T. Ruf, M. Cardona, C. T. Lin, J. Wrzesinski, M. Steube, K. Reimann, J.-C. Merle, and M. Joucla, Phys. Rev. B **57**, 15183 (1998).

[57] Y. Toyozawa, Prog. Theor. Phys. **20**, 53 (1958).

[58] M. Schreiber and Y. Toyozawa, J. Phys. Soc. Jpn. **51**, 1528 (1982).

[59] M. R. Filip, C. E. Patrick, and F. Giustino, Phys. Rev. B **87**, 205125 (2013).

[60] K. T. Butler, S. McKechnie, P. Azarhoosh, M. van Schilfgaarde, D. O. Scanlon, and A. Walsh, Appl. Phys. Lett. **108**, 112103 (2016).

[61] F. Bechstedt, *Many-Body Approach to Electronic Excitations: Concepts and Applications*, 1st ed. (Springer, 2015).

[62] W. G. Schmidt, S. Glutsch, P. H. Hahn, and F. Bechstedt, Phys. Rev. B **67**, 085307 (2003).

[63] S. Albrecht, L. Reining, R. Del Sole, and G. Onida, Phys. Rev. Lett. **80**, 4510 (1998).

[64] J. Furthmüller, F. Fuchs, and F. Bechstedt, in *Indium Nitride and Related Alloys*, 1st ed., edited by T. D. Veal, C. F. McConville, and W. J. Schaff (CRC Press, 2010), Chap. 8.4.

[65] P. Y. Yu and M. Cardona, *Fundamentals of Semiconductors*, 4th ed. (Springer, 2010).

[66] C. B. Duke and B. Segall, Phys. Rev. Lett. **17**, 19 (1966).

[67] J. Hermanson, Phys. Rev. Lett. **18**, 170 (1967).

[68] S. Adachi, *Properties of Group-IV, III-V and II-VI Semiconductors*, 1st ed. (Wiley, 2005).

[69] C. Macías, S. Lugo, Á. Benítez, I. López, B. Kharissov, A. Vázquez, and Y. Peña, Mater. Res. Bull. **87**, 161 (2017).

[70] S. C. Riha, A. A. Koegel, J. D. Emery, M. J. Pellin, and A. B. F. Martinson, ACS Appl. Mater. Interfaces **9**, 4667 (2017).

[71] L. Wan, C. Ma, K. Hu, R. Zhou, X. Mao, S. Pan, L. H. Wong, and J. Xu, J. Alloys Compd. **680**, 182 (2016).

[72] A. Hussain, R. Ahmed, N. Ali, F. K. Butt, A. Shaari, W. W. Shamsuri, R. Khenata, D. Prakash, and K. Verma, Superlattices Microstruct. **89**, 136 (2016).

[73] B. Zhu, X. Chen, and X. Cui, Sci. Rep. **5**, 9218 (2015).

[74] M. M. Ugeda, A. J. Bradley, S.-F. Shi, F. H. da Jornada, Y. Zhang, D. Y. Qiu, W. Ruan, S.-K. Mo, Z. Hussain, Z.-X. Shen, F. Wang, S. G. Louie, and M. F. Crommie, Nat. Mater. **13**, 1091 (2014).

[75] G. Zhang, A. Chaves, S. Huang, F. Wang, Q. Xing, T. Low, and H. Yan, Sci. Adv. **4**, eaap9977 (2018).

[76] B. Gil, D. Felbacq, and S. F. Chichibu, Phys. Rev. B **85**, 075205 (2012).

[77] M. Fox, *Optical Properties of Solids*, 2nd ed. (Oxford, 2010).

[78] J. L. Shay, B. Tell, L. M. Schiavone, H. M. Kasper, and F. Thiel, Phys. Rev. B **9**, 1719 (1974).

[79] M. I. Aroyo, A. Kirov, C. Capillas, J. M. Perez-Mato, and H. Wondratschek, Acta Crystallogr., Sect. A: Found. Crystallogr. **62**, 115 (2006).

[80] C. F. Klingshirn, *Semiconductor Optics*, 4th ed. (Springer, Heidelberg, 2012).

[81] N. Kuroda, I. Munakata, and Y. Nishina, Solid State Commun. **33**, 687 (1980).

[82] A. R. Beal, J. C. Knights, and W. Y. Liang, J. Phys. C **5**, 3540 (1972).

[83] N. Saigal, V. Sugunakar, and S. Ghosh, Appl. Phys. Lett. **108**, 132105 (2016).

[84] H. Yu, X. Cui, X. Xu, and W. Yao, Natl. Sci. Rev. **2**, 57 (2015).

[85] N. C. Giebink, G. P. Wiederrecht, M. R. Wasielewski, and S. R. Forrest, Phys. Rev. B **83**, 195326 (2011).

[86] M. Born and E. Wolf, *Principles of Optics: Electromagnetic Theory of Propagation, Interference and Diffraction of Light*, 7th ed. (Cambridge University Press, 2000).